Geometrically necessary dislocation structure organization in FCC bicrystal subjected to cyclic plasticity

T. Mayama, T. Ohashi, R. Kondou

PII: S0749-6419(09)00014-X
DOI: 10.1016/j.ijplas.2009.02.001
Reference: INTPLA 1215

To appear in: *International Journal of Plasticity*

Received Date: 3 July 2008
Revised Date: 25 January 2009
Accepted Date: 1 February 2009

Please cite this article as: Mayama, T., Ohashi, T., Kondou, R., Geometrically necessary dislocation structure organization in FCC bicrystal subjected to cyclic plasticity, *International Journal of Plasticity* (2009), doi: 10.1016/j.ijplas.2009.02.001

(a) Article title:

Geometrically necessary dislocation structure organization in FCC bicrystal subjected to cyclic plasticity

(b) Author names:

T. Mayama[a, *], T. Ohashi[b], R. Kondou[c]

(c) Affiliations:

[a] Kumamoto University, 2-39-1, Kurokami, Kumamoto 860-8555, Japan

[b] Kitami Institute of Technology, 165 Koen-cho, Kitami-shi, Hokkaido 090-8507, Japan

[c] University of the Ryukyus, 1 Senbaru, Nishihara-cho, Nakagami-gun, Okinawa 903-0213, Japan

(d) Abstract:

Crystal plasticity finite element analysis of cyclic deformation of compatible type FCC bicrystals are performed. The model specimen used in the analysis is a virtual FCC bicrystal with an isotropic elastic property; therefore, the effect of constraint due to elastic incompatibility does not appear. The results of the analysis show the

strain-amplitude-dependence of both the organization of the GND structure and the stress-strain behavior. The calculated stress-strain curve with the largest strain amplitude shows additional cyclic hardening. The microscopic mechanisms of the strain-amplitude-dependent organization of the GND structure and additional cyclic hardening behavior are discussed in terms of the activation of secondary slip system(s). Finally, the effects of the elastic anisotropy, the lattice friction stress and the interaction between dislocations are also argued.

(e) Keywords:

A. dislocation; A. grain boundaries; B. crystal plasticity; B. cyclic loading; C. finite elements

(f) the corresponding author's telephone and fax numbers an e-mail address

Telephone number : +81-96-342-3877

Fax number : +81-96-342-3877

e-mail address : mayama@kumamoto-u.ac.jp

1. Introduction

The main process of fatigue failure of metallic materials consists of fatigue crack initiation and crack propagation, both of which are closely related to local shear slip (local plastic deformation) due to local stress concentration (Suresh, 1998; Polak, 1991). In order to understand the essential mechanism of fatigue, therefore, the heterogeneity of plastic deformation at the micro-scale and the evolution of microstructure during cyclic loading must be clarified quantitatively. Although it is difficult to experimentally observe the evolution of microstructure, recent computational investigations show that the crystal plasticity finite element method could be used for quantitative evaluation of heterogeneous accumulation of crystallographic slips (Mayama et al., 2008; Xie et al., 2004; Manonukul and Dunne, 2004; Dunne et al., 2007; Sinha and Ghosh, 2006; Cheong, 2008; Mayeur et al., 2008; Shenoy et al., 2008; Morrissey et al., 2001; Goh et al., 2001; Bennett and McDowell, 2003; Turkmen et al., 2002; Goh et al., 2003, 2006; Shenoy et al., 2007) while the phenomenological approaches have also been extensively investigated the macro-scopic aspects of the cyclic plasticity (Mayama et al., 2007; Chaboche, 2008; Rahman et al., 2008; Moosbrugger et al., 2008; Hassan et al., 2008, Zhang and Jiang, 2008). Recently, McDowell (2007) outlined computational approaches to microstructure-sensitive fatigue

analysis and presented several directions for future research in computational fatigue modeling.

Fatigue cracks can nucleate inside the materials due to local stress concentration caused by grain boundaries, twin boundaries, and inclusions as well as at the surface of a material due to PSB formation during cyclic loading (Suresh, 1998; Polak, 1991 Kimura et al., 2004; Li et al., 2004; Yang et al., 2007). Recent developments in microscopic measurement methods for surface roughness and crystallographic texture provide considerable insight into fatigue crack initiation. Kimura et al. (2004) discussed the effect of microstructure and crystallographic orientation on fatigue crack initiation in ultrafine-grained steel using AFM and EBSP. Li et al. (2004) and Yang et al. (2007) observed the dislocation structure in copper bicrystals by using an electron channelling contrast technique in the SEM. However, the difficulty of experimental measurement and direct observation of the process inside the material has led to a lack of understanding of the micro-scale mechanism of fatigue crack initiation in the material. In this study, therefore, heterogeneous deformation near the grain boundary of FCC bicrystal is estimated quantitatively by means of crystal plasticity finite element analysis. Also, the evolution of the geometrically necessary dislocation (GND) structure during cyclic loading is numerically predicted. The mechanism of the

strain-amplitude-dependent evolution of the GND structure is discussed in terms of the activation of slip systems. The present calculation results also show strain-amplitude-dependent additional cyclic hardening. These numerical results are compared with the experimental results for copper bicrystals subjected to cyclic loading conducted by Hu et al. (1996a, b) and Hu and Wang (1998). The effects of elastic anisotropy, the lattice friction stress and the interactions of dislocations between different slip systems on the evolution of the GND structure are also discussed.

2. Procedure for crystal plasticity analysis

2.1 Constitutive equations

In this study, a 3-dimensional crystal plasticity finite element analysis code developed by Ohashi (1987, 1990a, 1997, 2004, 2005) was employed. Ohashi et al. (2007) showed that this model can be modified for scale-dependent yield stress in polycrystalline metals using results of discrete dislocation dynamics analysis. Recently, this model successfully predicted the experimental results of GND accumulation near the grain boundary of nickel bicrystal (Ohashi et al. 2008). The constitutive equations implemented in the software code are shown below.

The critical resolved shear stress $\theta^{(n)}$ on slip system n is given by the Schmid

law as

$$\theta^{(n)} = P_{ij}^{(n)} \sigma_{ij} , \tag{1}$$

where σ_{ij} denotes the stress tensor. $P_{ij}^{(n)}$ is the Schmid tensor of slip system n defined by

$$P_{ij}^{(n)} = \frac{1}{2}\left(v_i^{(n)} b_j^{(n)} + v_j^{(n)} b_i^{(n)} \right), \tag{2}$$

where $v_i^{(n)}$ and $b_i^{(n)}$ are the slip plane normal and the slip direction, respectively. The increment of the critical resolved shear stress is written as follows:

$$\dot{\theta}^{(n)} = \sum_m h^{(nm)} \dot{\gamma}^{(m)} . \tag{3}$$

Here, $h^{(nm)}$ and $\dot{\gamma}^{(m)}$ denote the strain hardening coefficient and the increment of the plastic shear strain on slip system m.

Assuming that the deformation is small and rotation of the crystal orientation is ignored, the constitutive equation for slip deformation is given by

$$\dot{\varepsilon}_{ij} = \left[S_{ijkl}^{e} + \sum_n \sum_m \left\{ h^{(nm)} \right\}^{-1} P_{ij}^{(n)} P_{kl}^{(m)} \right] \dot{\sigma}_{kl} , \tag{4}$$

where S_{ijkl}^{e} denotes the elastic compliance, and the summation is made over the active slip systems. We solve the deformation with a rate-independent plasticity formulation.

The following Bailey-Hirsch type model of the critical resolved shear stress is used,

$$\theta^{(n)} = \theta_0 + \sum_m \Omega^{(nm)} a \mu \tilde{b} \sqrt{\rho_S^{(m)}} , \tag{5}$$

where θ_0, a, μ, $\tilde{b}$ and $\rho_S^{(m)}$ denote the lattice friction term, a numerical factor on

the order of 0.1, the elastic shear modulus, the magnitude of the Burgers vector and the statistically stored dislocation (SSD) density that accumulates on slip system m, respectively. By substituting the derivation of Eq.(5) into Eq.(3), the strain hardening coefficient $h^{(nm)}$ in Eq.(3) is specified. In this study, the initial SSD density $\rho_S^{(m)}$ is set to be $10^9\left[m^{-2}\right]$ for all slip systems. The interaction of slip systems n and m is controlled by the interaction matrix $\Omega^{(nm)}$ in Eq.(5) (Ohashi, 1987, 1990a, 2004, 2005; Ohashi et al., 2007). In all the calculation except for Section 4.5 $\Omega^{(nn)}=1$ for the diagonal components and $\Omega^{(nm)}=1.01$ for the off-diagonal components are used to represent a nearly isotropic hardening characteristic for every slip system. The effect of the anisotropic hardening, when the off-diagonal components are changed, is discussed in Section 4.5. The increment in the SSD density on slip system n is given as follows:

$$\dot{\rho}_S^{(n)}=\frac{c\dot{\gamma}^{(n)}}{\tilde{b}L^{(n)}}, \tag{6}$$

where c is a numerical coefficient on the order of 1 and $L^{(n)}$ is the mean free path of dislocations on slip system n defined as

$$L^{(n)}=\frac{c^*}{\sqrt{\sum_m \omega^{(nm)}\left(\rho_S^{(m)}+\left\|\rho_G^{(m)}\right\|\right)}}, \tag{7}$$

where c^* and $\omega^{(nm)}$ are a material constant of the order of 10-100 (Kuhlmann-Wilsdorf, 1989) and the weight matrix, respectively. In this study, when $n=m$ or slip systems n and m are co-planar the components of the weight matrix $\omega^{(nm)}$ are assumed to be 0. Otherwise components of $\omega^{(nm)}$ are assumed to be 1. In Section 4.5, the effect of the weight matrix on the evolution of GND density norm distribution is evaluated. $\left\|\rho_G^{(m)}\right\|$ denotes the norm of geometrically necessary dislocation (GND) density on slip system m defined as

$$\left\|\rho_G^{(m)}\right\| = \sqrt{\left(\rho_{G,edge}^{(m)}\right)^2 + \left(\rho_{G,screw}^{(m)}\right)^2}, \tag{8}$$

where the edge and screw components are defined by the strain gradient (Ohashi, 1997, 2004, 2005):

$$\rho_{G,edge}^{(m)} = -\frac{1}{\tilde{b}}\frac{\partial \gamma^{(m)}}{\partial \xi}, \qquad \rho_{G,screw}^{(m)} = \frac{1}{\tilde{b}}\frac{\partial \gamma^{(m)}}{\partial \zeta}. \tag{9}$$

Here, ξ and ζ denote directions parallel and perpendicular to the slip plane, respectively.

The material parameters in the constitutive equations and elastic compliance used in this study are shown in Table 1. The typical material parameters were chosen from previous studies (Ohashi, 2004, 2005; Ohashi et al. 2007). The elastic compliance is used to obtain elastic isotropy, so grain boundary constraint due to elastic incompatibility (Hook and Hirth, 1967) does not appear. In Sections 4.3, 4.4 and 4.5,

the effects of material parameters of elastic anisotropy, lattice friction stress in Eq.(5) and the components of interaction matrix in Eq.(5) and weight matrix in Eq.(7) on the evolution of GND density norm distribution are discussed.

2.2 Finite element analysis model

The geometry of the present analysis model is shown in Fig.1. The size of the model is $20\times20\times2\mu m$. The model is uniformly divided into $20\times20\times4$ elements using a brick-shaped element with eight nodes. The effect of the mesh resolution is discussed later. All the nodes on the bottom surface are fixed in the Y-direction. The tensile or compressive loading for cyclic loading is given by the displacement in the Y-direction of all the nodes on the top surface. The boundary conditions on lateral surfaces of this model are traction free. Consequently, this model predicts the accumulation of GNDs induced by the interaction between the bicrystal and the un-modeled rigid crystals placed over and beneath this bicrystal because the top and bottom surfaces of this model are constrained to be flat by the rigid ones. In real polycrystals, the third and fourth crystals will have finite rigidities and thus deform accordingly however, the displacement field in the bicrystal part will be similar to that obtained with rigid crystals.

The stress field induced by this constraint is analogous to that for the case when wedge type disclinations are introduced at the upper and bottom ends of the grain boundary (Kondou and Ohashi 2004; Kondou et al., 2008). Thus, the deformation of the present model of bicrystal is essentially similar to that in a model with the third and fourth grains above and beneath the bicrystal except for the effect of the additional deformations in the third grain. The increase in the number of grains leads to complex phenomena during cyclic loading, which makes difficult to understand the dominant mechanism. For that reason, the present model is used to simulate the multi-body interaction near grain boundary triple junctions in polycrystals although the crystals over and beneath the bicrystal do not deform at all. In this case, the choice of crystal orientations of each crystal of the bicrystal affects the results of the GND accumulation significantly. The selection of the crystal orientations in this study is discussed as follows.

In this study, the Schmid-Boas notation for the twelve slip systems in FCC metal is defined as shown in Table 2. The relationship between the crystal coordinate and sample coordinate is given as follows:

$$\begin{pmatrix} [100] \\ [010] \\ [001] \end{pmatrix} = \begin{pmatrix} -\sin\theta\cos\phi & \cos\theta \\ \cos\kappa\sin\phi + \cos\theta\sin\kappa\cos\phi & \sin\theta\sin\kappa \\ -\sin\kappa\sin\phi + \cos\theta\cos\kappa\cos\phi & \sin\theta\cos\kappa \end{pmatrix}$$

$$\begin{pmatrix} \sin\theta\sin\phi \\ \cos\kappa\cos\phi - \cos\theta\sin\kappa\sin\phi \\ -\sin\kappa\cos\phi - \cos\theta\cos\kappa\sin\phi \end{pmatrix} \begin{pmatrix} x \\ y \\ z \end{pmatrix} \tag{10}$$

where κ, θ and ϕ show Euler angles as seen in Fig.2. Selected crystal orientation is $(\kappa,\theta,\phi) = (77.0°, 24.705°, 77.636°)$ for Grain 1 and $(\kappa,\theta,\phi) = (77.0°, 24.705°, 257.636°)$ for Grain 2 (Kondou and Ohashi, 2007). The Schmid factors of these grains for loading at the y-axis as shown in Table 2 are identical because the orientation of Grain 2 is obtained by rotating the orientation of Grain 1 180° about the y-axis. The slip directions and the slip plane normal of the primary slip system B4 $(11\bar{1})[101]$ of both grains lie parallel to the $x-y$ plane. Therefore, the angle α in Fig.1 between the slip plane and y-axis direction for both grains becomes the same value, 44.856°. The reason for this selection of angle is schematically shown in Fig.3. When the angle α is 45°, the components of the slip plane normal vector and the slip direction vector on the primary slip system are $\mathbf{v}^{(primary)} = (1/\sqrt{2}, 1/\sqrt{2}, 0)$ and $\mathbf{b}^{(primary)} = (-1/\sqrt{2}, 1/\sqrt{2}, 0)$, respectively. Therefore, the Schmid tensor, given by Eq.(2), of the primary slip system becomes

$$\mathbf{P}^{(primary)} = \begin{pmatrix} -1/2 & 0 & 0 \\ 0 & 1/2 & 0 \\ 0 & 0 & 0 \end{pmatrix}. \tag{11}$$

When only the primary slip system is activated, the macroscopic plastic strain rate is calculated as follows.

$$\dot{\boldsymbol{\varepsilon}}^{p} = \mathbf{P}^{(primary)}\dot{\gamma}^{(primary)}. \tag{12}$$

From Eqs.(11) and (12), it can be found that the deformed geometry becomes macroscopically rectangular because all the macroscopic shear strain rates become zero when the elastic isotropy is assumed. Therefore, if the rotation of crystal orientation is ignored, there is no constraint between the two grains in the bicrystal as shown in Fig.3a. In contrast to this, when the angle α deviates from 45°, crystal grains deform into parallelograms. Therefore, there is deformation constraint on the grain boundary in the bicrystal, which induces GNDs on the grain boundary as shown in Fig.3b (Kondou and Ohashi, 2007). Consequently, the deformation can be heterogeneous even during axial loading (Ohashi, 1990b).

3. Results

3.1 Effect of finite element mesh resolution

Fig.4a, b and c shows the GND norm density distributions of the model deformed up to 0.25% in tensile loading with finite element mesh resolutions of $20\times20\times4$,

$30\times30\times4$ and $40\times40\times4$ elements, respectively. The maximum and minimum values of GND norm density are also shown in Fig.4. The range of contour is adjusted for each resolution, so the qualitative difference can be compared. Although the maximum value of GND norm density increases with the increase in number of elements used in the finite element model, the overall GND norm density distributions for each resolution are qualitatively similar. The purpose of this study is not to estimate the quantity of GND density but to clarify the evolution mechanism of the dislocation structure. Therefore for the sake of time efficiency in this study, the model with the $20\times20\times4$ element is used for cyclic loading calculations.

3.2 Strain-amplitude-dependent organization of the GND structure due to cyclic loading

Fig.5 shows the evolution of GND norm density distribution on the primary slip system during cyclic loading up to 10 cycles. The ranges of contour are adjusted to the maximum and minimum values for strain amplitude during the 10 cycles, so the normalized density distribution after 10 cycles is as illustrated in Fig.5d. The model with strain amplitude +/- 0.01% does not show any significant change in GND norm density structure during cyclic loading, although the models with strain amplitudes larger than +/- 0.05% show an increase in the GND norm density during cyclic loading.

The density distributions shown in Fig.5d are qualitatively different. These results indicate that not only the absolute value of GND density but also the morphology of GND structure change depending on the strain amplitude.

4. Discussion

4.1 Mechanism of strain-amplitude-dependent evolution of GND density distribution

Fig.6a-e shows the evolution of GND norm density distributions on the primary (B4) and a secondary (A3) slip systems during the 1st cycle with strain amplitude 0.01% at strain 0.002%, 0.006%, 0.01%, 0.008% and -0.01%, respectively. The results in Fig.6d and e illustrate the distribution after stress reversal. These figures show that GND accumulates only on the primary slip system. Fig.7a-e shows the evolution of GND norm density distribution on the primary (B4) and the secondary (A3) slip systems during the 1st cycle with strain amplitude 0.05% at strain 0.01%, 0.03%, 0.05%, 0.04% and -0.05%, respectively. These figures show that GNDs on the secondary slip system (A3) accumulates at the top of the center of distribution just after loading reversal. Fig.8a-e shows the evolution of GND norm density distributions on the primary (B4) and the secondary (A3) slip systems during the 1st cycle with strain amplitude 0.25% at strain 0.05%, 0.15%, 0.25%, 0.2% and -0.25%, respectively.

These figures show that GNDs on the secondary slip system (A3) accumulates not only at the top of the center but also at the bottom of the center. Fig.9a-e shows the evolution of GND norm density distributions on the primary (B4) and the secondary (A3) slip systems during the 1st cycle with strain amplitude 1.0% at strain 0.2%, 0.6%, 1.0%, 0.8% and -1.0%, respectively. These figures show that GNDs on the secondary slip system (A3) accumulates from the top through the bottom of the center. This accumulation corresponds to the activation of the secondary slip system near the grain boundary.

From these results shown in Figs.6-9, the strain-amplitude-dependency of GND density distribution is assumed to evolve through the following mechanism. That is, the larger strain amplitude leads to a more significant activation of secondary slip systems and accumulation of GNDs due to constraint near the grain boundary. The activation of secondary slip systems contributes also to an increase in SSD density on the primary slip system due to the decrease in the mean free path of dislocations as shown in Eq.(7). Because the increase in SSD density results in an increase in flow stress, a heterogeneous stress field is induced. Consequently, the heterogeneous GND structure evolves gradually during cyclic loading. In contrast to this, with sufficiently small strain amplitude, secondary slip systems cannot be activated and SSD density

increases uniformly because GNDs on the primary slip system does not affect the mean free path of dislocations on the same slip system. The physical interpretation of this process is that locally accumulated dislocations on secondary slip system(s) interrupts slips on the primary slip system. Consequently, the shear slip distribution on the primary slip system becomes heterogeneous, which corresponds to the evolution of the GND structure on the primary slip system.

Hu et al. (1996a, b) conducted cyclic loading experiments and surface observations for copper bicrystals. The experimental results showed that saturation stress increases with strain amplitude. They concluded that the activation of secondary slip systems in the vicinity of the grain boundary with the increase in the strain amplitude contributes to the increase in saturation stress. Based on the experimental results for copper bicrystal subjected to fatigue deformation, Hu and Wang (1998) reported that the grain boundary effect was not observed at low strain amplitude, while the effect was significant when the amplitude was high. They attributed the difference to large incompatible stresses at the grain boundary. Although the number of loading cycles in these experimental studies is much larger than that in the present simulations and the elastic isotropy, zero lattice friction stress and the same interaction between dislocations is assumed in the calculation, there are remarkable similarities such as the

grain boundary effects and the strain-amplitude-dependent activation of secondary slip systems.

4.2 Strain-amplitude-dependent additional cyclic hardening

Fig.10 shows the relationships between the peak stresses at each cycle and the accumulated plastic strain during cyclic loading. The inset in Fig.10 shows an enlargement of the part within the square. In these figures, cyclic loading with larger strain amplitude shows a slight additional cyclic hardening. The mechanism of this additional cyclic hardening is explained by the additional increase in SSD density due to multiple slip activation and the decrease in the mean free path of dislocation, similar to the mechanism of the strain-amplitude-dependent evolution of GND density as explained in Section 4.1.

The experimental results for bicrystal copper subjected to cyclic loading conducted by Hu et al. (1996a, b) show similar additional cyclic hardening with an increase in strain amplitude. This type of strain-amplitude-dependent additional cyclic hardening can also be seen in experiments on polycrystalline materials (Tanaka et al., 1985; Kang et al., 2003). The relationship between the present simulated results with bicrystal and the experimental results for polycrystalline materials has not been clarified.

Further computational investigation and experimental observation are needed to explain the mechanism of the additional cyclic hardening.

4.3 The effect of the elastic anisotropy on the evolution of the GND structure

In this section, the effect of elastic anisotropy is discussed. The anisotropic elastic compliances for copper used in this section are $S_{11} = 1.4995 \times 10^{-11}$, $S_{12} = -0.6282 \times 10^{-11}$ $S_{44} = 1.3263 \times 10^{-11} \left[m^2 / N \right]$ (Simmons and Wang, 1971), and the anisotropy ratio $2\left(s_{11} - s_{12}\right)/s_{44}$ is 3.2085. Fig.11 shows the evolution of GND norm density distribution on the primary slip system. Comparing to the results in Fig.11 with the isotropic elastic compliances shown in Fig.5, the GND norm density structures with smaller strain amplitudes show clearly different morphology although the overall distributions in the results with the larger strain amplitudes are similar. The results with the strain amplitudes +/- 0.01% and +/- 0.05% in Fig.11 show the GNDs accumulate near the grain boundary. Fig.12 shows the relationships between the normalized average GND density norm and the number of cycles. For the normalization, the average GND density norm is divided by the average GND density norm at 10^{th} cycle of the result with the anisotropic elastic compliance. This figure shows that the average GND density norm of all the results, except for the strain

amplitude +/- 0.01% with the isotropic elastic compliance, increases with the number of cycles. The increase in the average GND density norm is larger in the result with anisotropic elastic compliances. During the cyclic loading of the strain amplitude +/-0.01% with the anisotropic elastic compliances the secondary slip system is activated although the cyclic loading of the strain amplitude +/- 0.01% with the isotropic elastic compliances shows that only the primary slip system is activated. That is, the elastic anisotropy leads to more significant activation of secondary slip system(s), which results in the more significant increase in the average GND density norm. Therefore, in the present calculations, the mechanism of the evolution of GND structure for the model with elastic anisotropy can be explained by the same concept in Section 4.1.

4.4 The effect of the lattice friction stress on the evolution of the GND structure

In this section, the effect of lattice friction stress θ_0 in Eq.(5) is discussed. Fig.13 shows the evolution of GND norm density distribution during cyclic loading with the strain amplitude +/- 0.05% and +/- 0.25% using the lattice friction stress $\theta_0 = 0.4MPa$ and $\theta_0 = 4MPa$. The ranges of contours are the same to the results with $\theta_0 = 0MPa$ in Fig.5. The results with strain amplitude 0.25% show that the increase in the lattice friction stress θ_0 results in less evolution of GND density norm distribution. Fig.14

shows the relationship between the average GND norm density on the primary slip system and the number of cycles. This figure shows that the smaller lattice friction stress leads to more increase in average GND norm density. The results with the lattice friction stress $\theta_0 = 0.4MPa$ and $\theta_0 = 4MPa$ in Fig.14a, and $\theta_0 = 4MPa$ in Fig.14b show almost no increase in average GND norm density. It was confirmed that the secondary slip system was not activated in these conditions. That is, due to the high lattice friction stress the critical resolved shear stress (CRSS) is increased, which results in the less activation of secondary slip system and the less evolution of GND structure.

4.5 The effect of the interactions of dislocation between different slip systems

In this section, to confirm the effect of the off-diagonal components of interaction matrix $\Omega^{(nm)}$ in Eq.(5) and the off-diagonal components except for co-planar components of weight matrix $\omega^{(nm)}$ in Eq.(7), the values in table 3 are used in the calculation. Fig.15 shows the evolution of GND norm density distribution during cyclic loading with the strain amplitude +/- 0.25%. The result with low value of the off-diagonal components of the interaction matrix and the weight matrix show the most significant evolution of GND norm density distribution. The lower values of the

off-diagonal components of the interaction matrix and the weight matrix leads to the more activation of secondary slip system, which results in significant evolution of GND structure.

5. Conclusion

Cyclic loading for symmetric bicrystal composed of FCC material with ideal elastic compatibility was investigated sing a crystal plasticity finite element method. The evolution of the geometrically necessary dislocation (GND) structure and strain-amplitude-dependent cyclic hardening were also examined. The following conclusions were obtained:

(i) Cyclic loading with larger strain amplitude led to more significant evolution of GND density. Qualitatively different evolutions of the GND structures dependent on the strain amplitude were also numerically predicted.

(ii) Cyclic loading with amplitude of +/- 1 % tension/compression strain showed distinct additional hardening compared to the results with smaller strain amplitude.

(iii) The strain amplitude dependency in cyclic plasticity was strongly affected by the activation of the secondary slip systems due to local stress near the grain

boundary. Larger strain amplitude induced larger internal stress due to the deformation constraint between crystal grains, and this led to more significant activation of secondary slip systems.

(iv) The effects of the elastic anisotropy, the lattice friction stress and the interaction between dislocations are investigated. The results show the slightly different behavior of the evolution of GND structure from the ideal model without these effects. However, all the results can be explained by the same mechanism to conclusion (iii), that is, the more significant activation of secondary slip system results in the more significant evolution of GND structure.

References

Bennet, V.P., McDowell, D.L., 2003. Polycrystal orientation distribution effects on microslip in high cycle fatigue. Int. J. Fatigue 25, 27-39.

Chaboche, J.L., 2008. A review of some plasticity and viscoplasticity constitutive theories. Int. J. Plasticity 24, 1642-1693.

Cheong, K.-S., 2008. The role of dislocations in cyclically deformed metal polycrystals. Current appl. phys. 8, 436-439.

Dunne, F.P.E., Wilkinson, A.J., Allen, R., 2007. Experimental and computational studies

of low cycle fatigue crack nucleation in a polycrystal. Int. J. Plasticity 23, 273-295.

Goh, C.-H., Wallace, J.M., Neu, R.W., McDowell, D.L., 2001. Polycrystal plasticity simulations of fretting fatigue. Int. J. Fatigue 23, S423-S435.

Goh, C.-H., Neu, R.W., McDowell, D.L., 2003. Crystallographic plasticity in fretting of Ti-6AL-4V. Int. J. Plasticity 19, 1627-1650.

Goh, C.-H., McDowell, D.L., Neu, R.W., 2006. Plasticity in polycrystalline fretting fatigue contacts. J. Mech. Phys. Solids 54, 340-367.

Hassan, T., Taleb, L., Krishna, S., 2008. Influence of non-proportional loading on ratcheting responses and simulations by two recent cyclic plasticity models. Int. J. Plasticity 24, 1863-1889.

Hook, R.E., Hirth, J.P., 1967. The deformation behavior of isoaxial bicrystals of Fe-3%Si. Acta Metall. 15, 535-551.

Hu, Y.M., Wang, Z.G., Li, G.Y., 1996a. Cyclic deformation behavior of a co-axial symmetrical copper bicrystal. Scripta Mater. 34, 331-336.

Hu, Y.M., Wang, Z.G., Li, G.Y., 1996b. Cyclic deformation behavior of copper bicrystals. Mater. Sci. Eng. A 208, 260-269.

Hu, Y.M., Wang, Z.G., 1998. Grain boundary effects on the fatigue deformation and cracking behavior of copper bicrystals. Int. J. Fatigue 20, 463-469.

Kang, G., Ohno, N., Nebu, A., 2003. Constitutive modeling of strain range dependent cyclic hardening. Int J Plasticity 19, 1801-1819.

Kimura, H., Akiniwa, Y., Tanaka, K., Tahara, Y., Ishikawa, T., 2004. JSME Int. J. A 47, 331-340.

Kondou, R., Ohashi, T., 2007. Crystal plasticity analysis of non-uniform deformation in symmetric type bicrystals under tensile load and formation of geometrically necessary dislocation bands. J Solid Mech. Mater. Eng. 1-1, 114-125.

Kondou, R. Ohashi, T., 2006. High density bands of GN dislocations formed by multi body interaction in compatible type multi crystal models. Key Eng. Mater. 340-341, 187-192.

Kondou, R. Ohashi, T., Miura, S., 2008. Relationship between micro-incompatibility and heterogeneity of dislocation density distribution in Cu-9at.% Al symmetric type bicrystal models under tensile loading. J. Comput. Sci. Technol. 2-1, 162-172.

Kuhlmann-Wilsdorf, D., 1989. Theory of plastic deformation:-properties of low energy dislocation structures. Mater Sci Eng A 113, 1-41.

Li, Y., Li, S.X., Li, G.Y., 2004. The dislocation structure evolution of deformation band and crack formation in a copper bicrystal with a perpendicular grain boundary. Mater. Sci. Eng. A 372, 221-228.

Manonukul, A., Dunne, F.P.E., 2004. High- and low-cycle fatigue crack initiation using polycrystal plasticity. Proc. R. Soc. Lond. A460, 1881-1903.

Mayama, T., Sasaki. K., Ishikawa, H., 2007. A constitutive model for cyclic viscoplasticity considering changes in subsequent viscoplastic deformation due to the evolution of dislocation structures. Int. J. Plasticity 23, 915-930.

Mayama, T., Sasaki, K., Kuroda, M., 2008. Quantitative evaluations for strain amplitude dependent organization of dislocation structures due to cyclic plasticity in austenitic stainless steel 316L. Acta Mater. 56, 2735-2743.

Mayeur, J.R., McDowell, D.L., Neu, R.W., 2008. Crystal plasticity simulations of fretting of Ti-6Al-4V in partial slip regime considering effects of texture. Comput Mater. Sci. 41, 356-365.

McDowell, D.L., 2007. Simulation-based strategies for microstructure-sensitive fatigue modeling. Mater. Sci. Eng. A 468-470, 4-14.

Moosbrugger J.C., Ratane, N.R., Morrison, D.J., 2008. Modeling aspects of low plastic strain amplitude multiaxial cyclic plasticity in conventional and ultrafine grain nickel. Int. J. Plasticity 24, 1837-1862.

Morrissey, R.J., McDowell, D.L., Nicholas, T., 2001. Microplasticity in HCF of Ti-6Al-4V. Int. J. Fatigue 23, S55-S64.

Ohashi, T., 1987. Computer simulation of non-uniform multiple slip in face centered cubic bicrystals. Trans. JIM 28, 906-915.

Ohashi, T., 1990a. Numerical analyses of deformation band evolution in face-centered cubic single crystals under tensile deformation. Mater. Trans. JIM 31, 456-462.

Ohashi, T., 1990b. Analysis of multiple slip in copper tricrystals. Colloque de Phys. Colloque C1, supple. au n1, Tome 51 C1-593-C1-598.

Ohashi, T., 1997. Finite-element analysis of plastic slip and evolution of geometrically necessary dislocations in fcc crystals. Philos. Mag. Letters 75, 51-57.

Ohashi, T., 2004. Three dimensional structures of the geometrically necessary dislocations in matrix-inclusion systems under uniaxial tensile loading. Int. J. Plasticity 20, 1093-1109.

Ohashi, T., 2005. Crystal plasticity analysis of dislocation emission from micro voids. Int J Plasticity 21, 2071-2088.

Ohashi, T., Kawamukai, M., Zbib, H., 2007. A multiscale approach for modeling scale-dependent yield stress in polycrystalline metals. Int J Plasticity 23, 897-914.

Ohashi, T., Barabash, R.I., Pang, J.W.L., Ice, G.E., Barabash, O.M., 2008. X-ray microdiffraction and strain gradient crystal plasticity studies of geometrically necessary dislocations near a Ni bicrystal grain boundary. Int J Plasticity, doi:

10.1016/j.ijplas.2008.04.009.

Polák J., 1991. Cyclic plasticity and low cycle fatigue life of metals. Materials science monographs; Vol.63. Amsterdam: Elsevier.

Rahman, S.M., Hassan, T., Corona, E., 2008. Evaluation of cyclic plasticity models in ratcheting simulation of straight pipes under cyclic bending and steady internal pressure. Int. J. Plasticity 24, 1756-1791.

Shenoy, M., Zhang, J., McDowell, D.L., 2007. Estimating fatigue sensitivity to polycrystalline Ni-base superalloy microstructures using a computational approach. Fatigue Fract. Eng. Mater. Struct. 30, 889-904.

Shenoy, M., Tjiptowidjojo, Y.T., McDowell, D., 2008. Microstructure-sensitive modeling of polycrystalline IN 100. Int J Plasticity 24, 1694-1730.

Simmons, G., Wang, H., 1971. Single crystal elastic constants and calculated aggregate properties, 2nd ed. The M.I.T. press.

Sinha, S., Ghosh, S., 2006. Modeling cyclic ratcheting based fatigue life of HSLA steels using crystal plasticity FEM simulations and experiments. Int. J. Fatigue 28, 1690-1704.

Suresh S., 1998. Fatigue of materials. 2nd ed. Cambridge: Cambridge University Press.

Tanaka, E., Murakami, S., Ooka, M., 1985. Effects of plastic strain amplitudes on non-proportional cyclic plasticity. Acta Mech. 57, 167-182.

Turkmen, H.S., Dawson, P.R., Matthew, P.M., 2002. The evolution of crystalline stresses of a polycrystalline metal during cyclic loading. Int. J. Plasticity 18, 941-969.

Xie, C.L., Ghosh, S., Groeber, M., 2004. Modeling cyclic deformation of HSLA steels using crystal plasticity. J. Eng. Mater. Technol. Trans. ASME 126, 339-352.

Yang, R.Q., Li, S.X., Zhang, Z.F., 2007. Cyclic deformation and dynamic compressive properties of copper bicrystals. Mater. Sci. Eng. A 466, 207-217.

Zhang, J., Jiang, Y., 2008. Constitutive modeling of cyclic plasticity deformation of a pure polycrystalline copper. Int. J. Plasticity 24, 1890-1915.

Tables

Figures

amplitude 1.0% (a) strain 0.2%; (b) strain 0.6%; (c) strain 1.0%; (d) strain 0.8% after loading reversal; (e) strain -1.0%

Fig.10 Strain amplitude dependency in cyclic hardening behavior

Fig.11 Evolution of GND norm density distribution on primary slip system (B4) during cyclic loading calculated with elastic anisotropy (a) at 1st peak stress; (b) after 1cycle; (c) after 5cycles; (d) after 10cycles

Fig.12 The effect of elastic anisotropy on the increase in average GND density norm

Fig.13 Evolution of GND norm density distribution on primary slip system (B4) during cyclic loading calculated with non-zero lattice friction stress θ_0 in Eq.(5) (a) at 1st peak stress; (b) after 1cycle; (c) after 5cycles; (d) after 10cycles

Fig.14 The effect of non-zero lattice friction stress on the increase in average GND density norm (a) strain amplitude 0.05%; (b) strain amplitude 0.25%

Fig.15 Effect of the off-diagonal component of interaction matrix $\Omega^{(n\neq m)}$ and the off-diagonal components except for co-planar of weight matrix $\omega^{(n\neq m)}$ on evolution of GND norm density distribution on primary slip system (B4) (a) at 1st peak stress; (b) after 1cycle; (c) after 5cycles; (d) after 10cycles

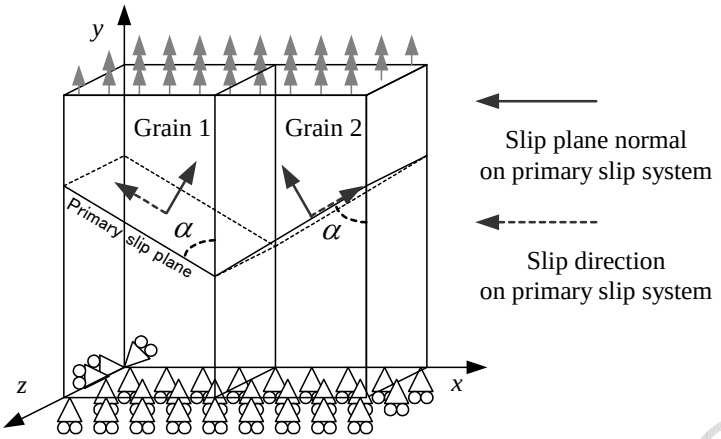

Fig.1 Schematic diagram of symmetric bi-crystal model

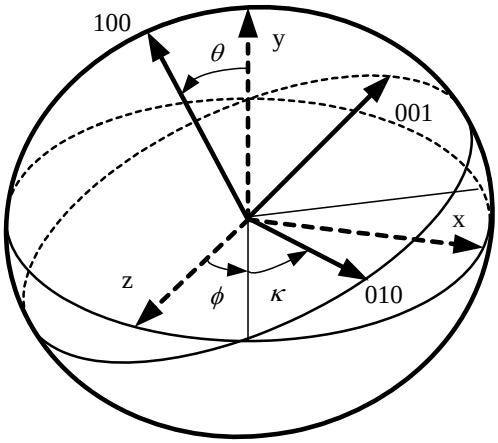

Fig.2 Definition of Euler angles

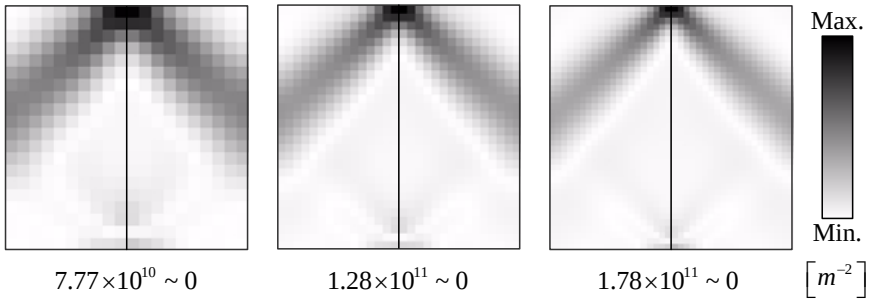

Fig.4 Effect of mesh resolution on GND norm density distribution

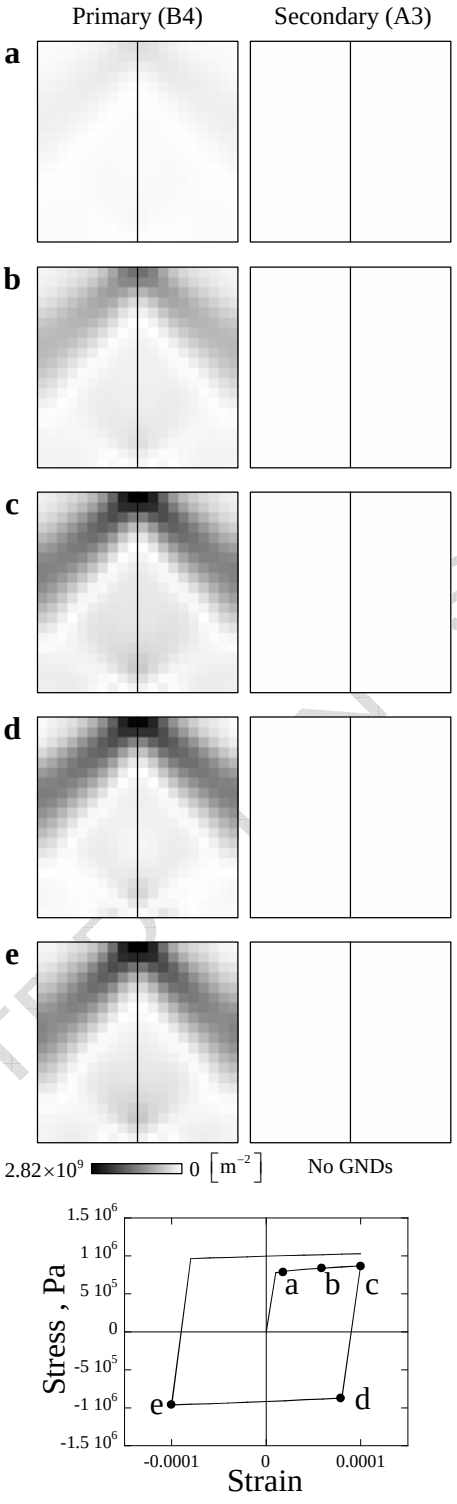

Fig.6 Evolution of GND norm density distribution during 1st cycle with strain amplitude 0.01% (a) strain 0.002%; (b) strain 0.006%; (c) strain 0.01%; (d) strain 0.008% after loading reversal; (e) strain -0.01%

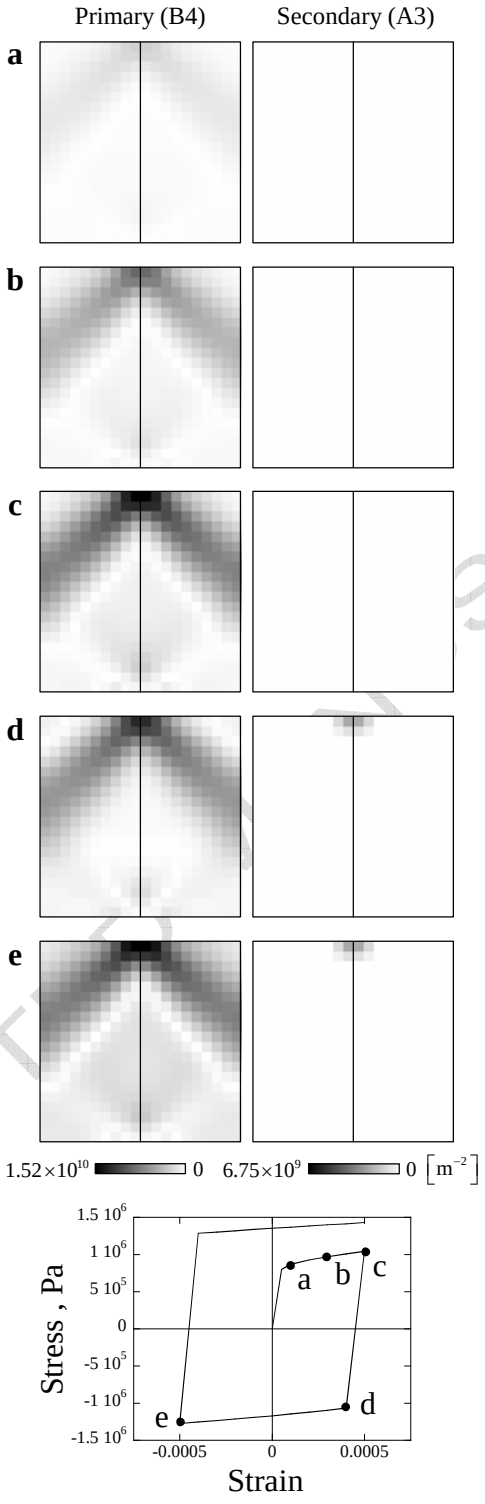

Fig.7 Evolution of GND norm density distribution during 1st cycle with strain amplitude 0.05% (a) strain 0.01%; (b) strain 0.03%; (c) strain 0.05%; (d) strain 0.04% after loading reversal; (e) strain -0.05%

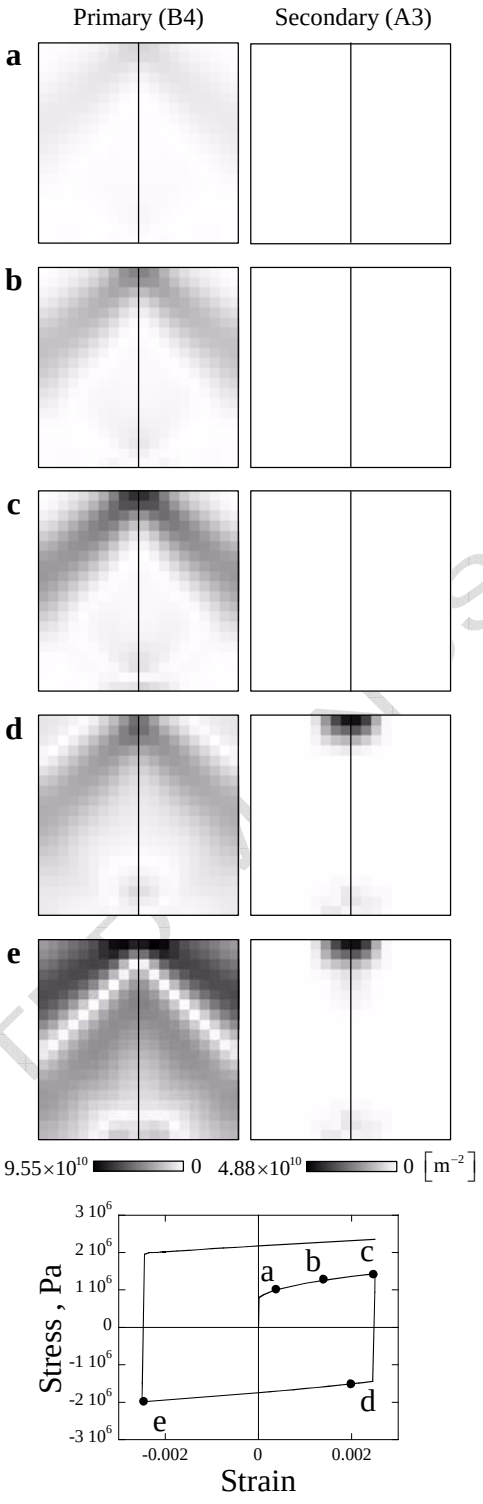

Fig.8 Evolution of GND norm density distribution during 1st cycle with strain amplitude 0.25% (a) strain 0.05%; (b) strain 0.15%; (c) strain 0.25%; (d) strain 0.2% after loading reversal; (e) strain -0.25%

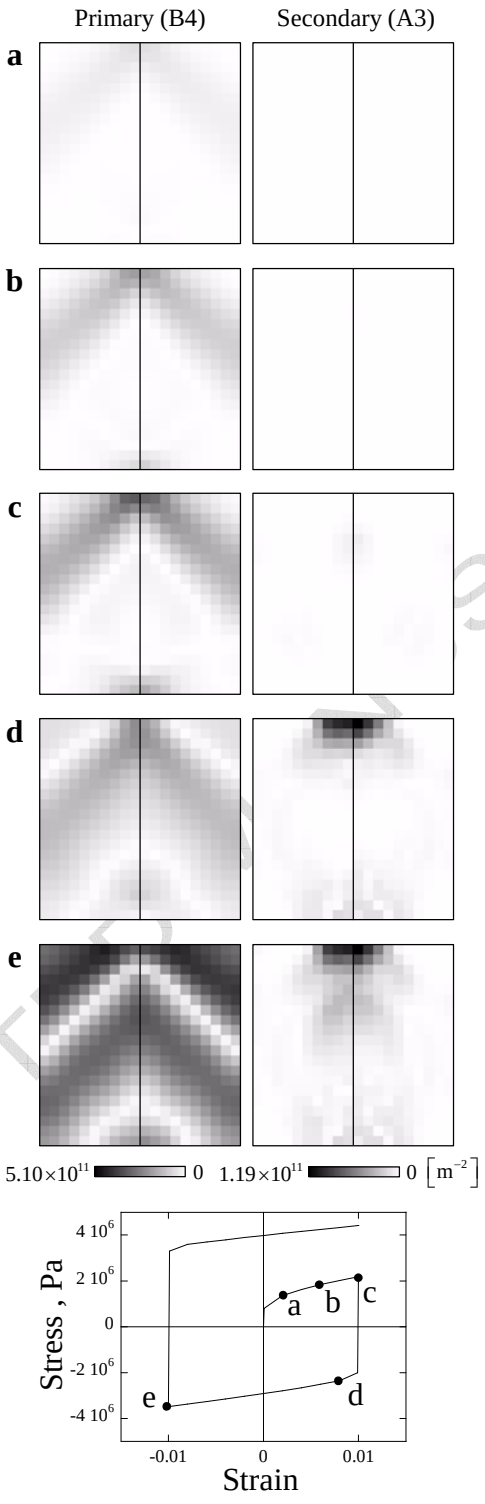

Fig.9 Evolution of GND norm density distribution during 1st cycle with strain amplitude 1.0% (a) strain 0.2%; (b) strain 0.6%; (c) strain 1.0%; (d) strain 0.8% after loading reversal; (e) strain -1.0%

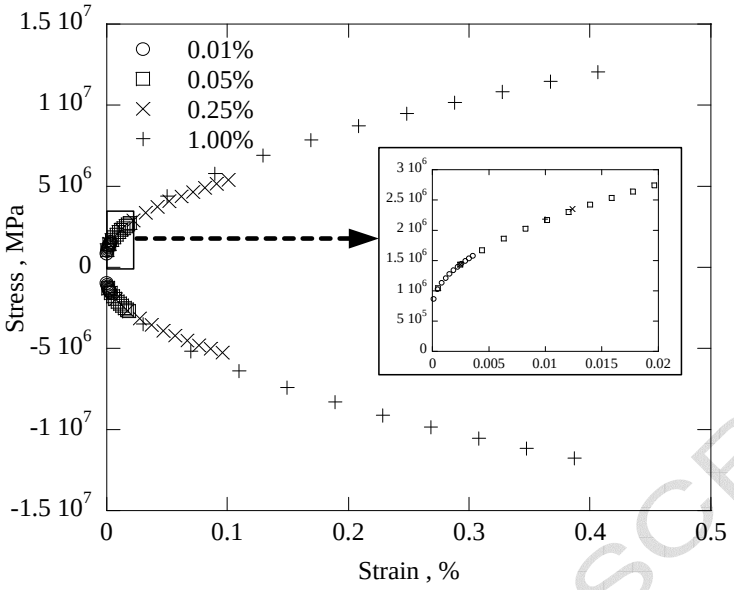

Fig.10 Strain amplitude dependency in cyclic hardening behavior

Table 1 Material parameters for the present analysis

Elastic compliances, $10^{-11}\,\mathrm{m}^2/\mathrm{N}$	$S_{11}=1.0$, $S_{12}=-0.25$, $S_{44}=2.5$
Shear modulus, $10^{11}\,\mathrm{Pa}$	$\mu=1/S_{44}=0.4$
Magnitude of Burgers vector, $10^{-10}\,\mathrm{m}$	2.556
Lattice friction stress θ_0, MPa (Eq.(5))	0
a in Eq.(5)	0.1
c in Eq.(6)	1.0
c^* in Eq.(7)	15

Table 2 Slip systems for FCC crystal and their Schmid-Boas notation and Schmid factor for loading in y-axis

No.	Schmid-Boas notation	Slip plane	Slip direction	Schmid factor for loading in y-axis	Remarks
1	A2	(111)	$[1\bar{1}0]$	0.288	
2	A6	(111)	$[01\bar{1}]$	0.180	
3	A3	(111)	$[10\bar{1}]$	0.469	
4	D1	$(\bar{1}11)$	$[110]$	0.219	
5	D6	$(\bar{1}11)$	$[01\bar{1}]$	0.052	
6	D4	$(\bar{1}11)$	$[101]$	0.167	
7	B2	$(11\bar{1})$	$[1\bar{1}0]$	0.250	
8	B5	$(11\bar{1})$	$[011]$	0.250	
9	B4	$(11\bar{1})$	$[101]$	0.500	Primary
10	C1	$(1\bar{1}1)$	$[110]$	0.320	
11	C5	$(1\bar{1}1)$	$[011]$	0.120	
12	C3	$(1\bar{1}1)$	$[10\bar{1}]$	0.198	

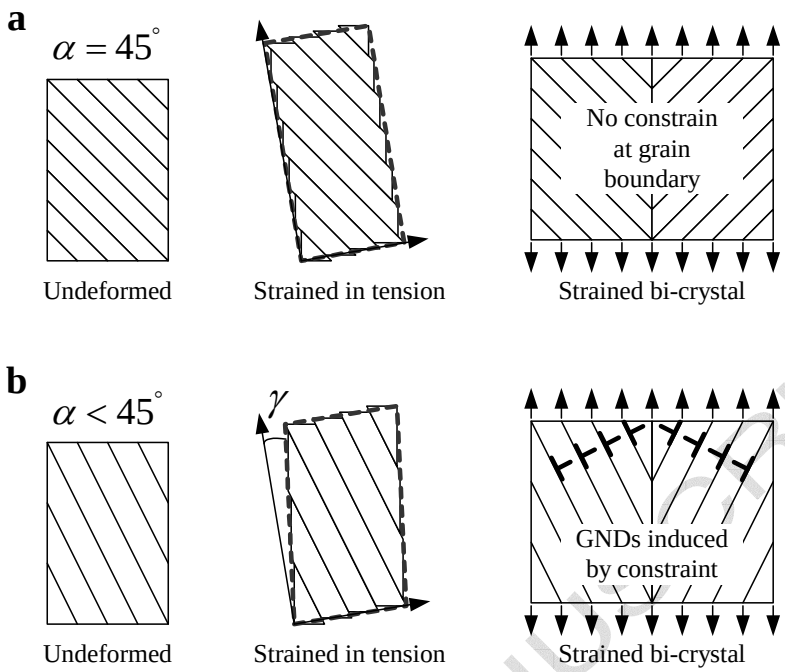

Fig.3 Crystal orientation dependent shear strain of single crystal and the effect on the interaction between two grains in symmetric bi-crystal

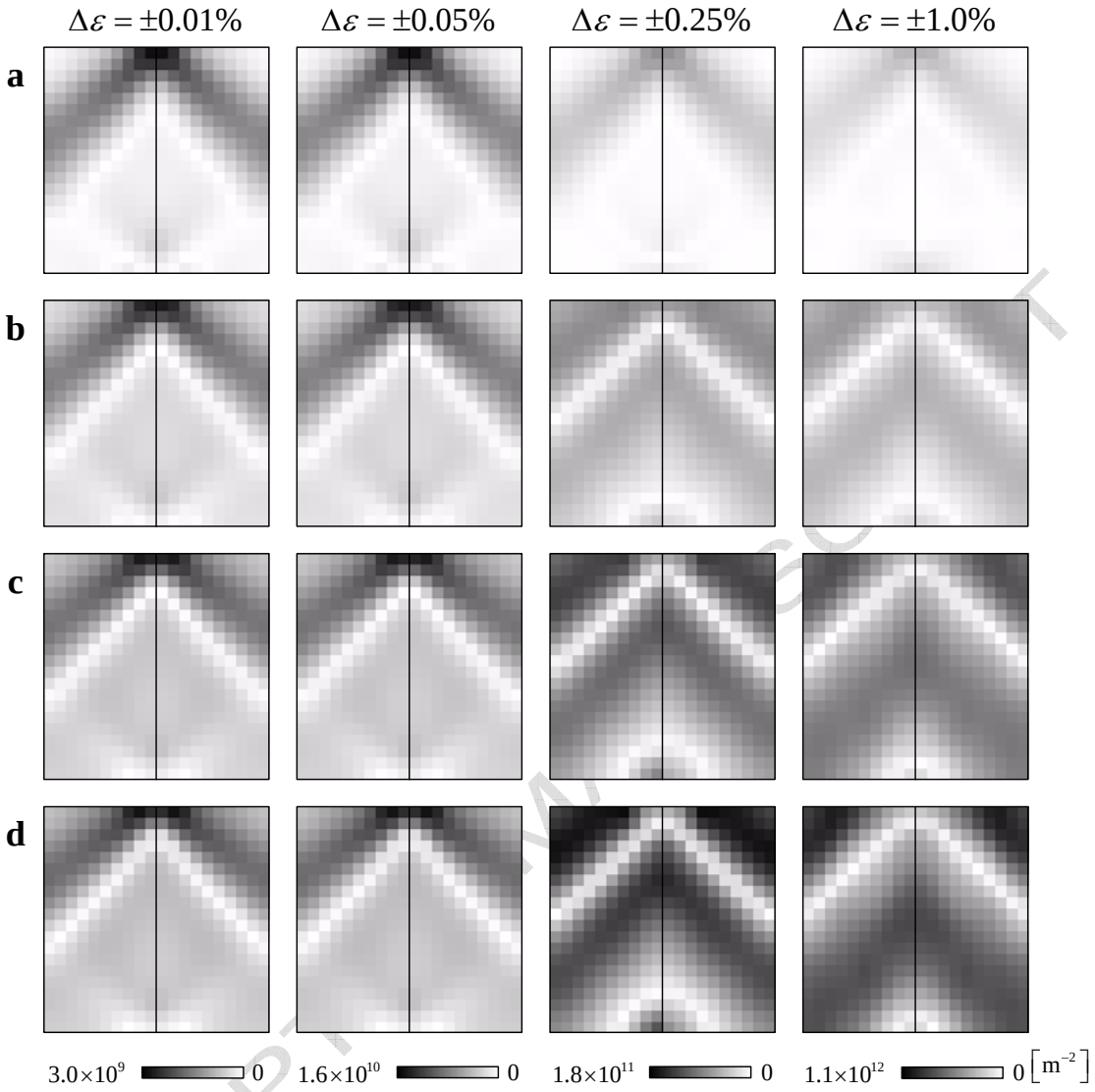

Fig.5 Evolution of GND norm density distribution on primary slip system (B4) during cyclic loading (a) at 1st peak stress; (b) after 1cycle; (c) after 5cycles; (d) after 10cycles.

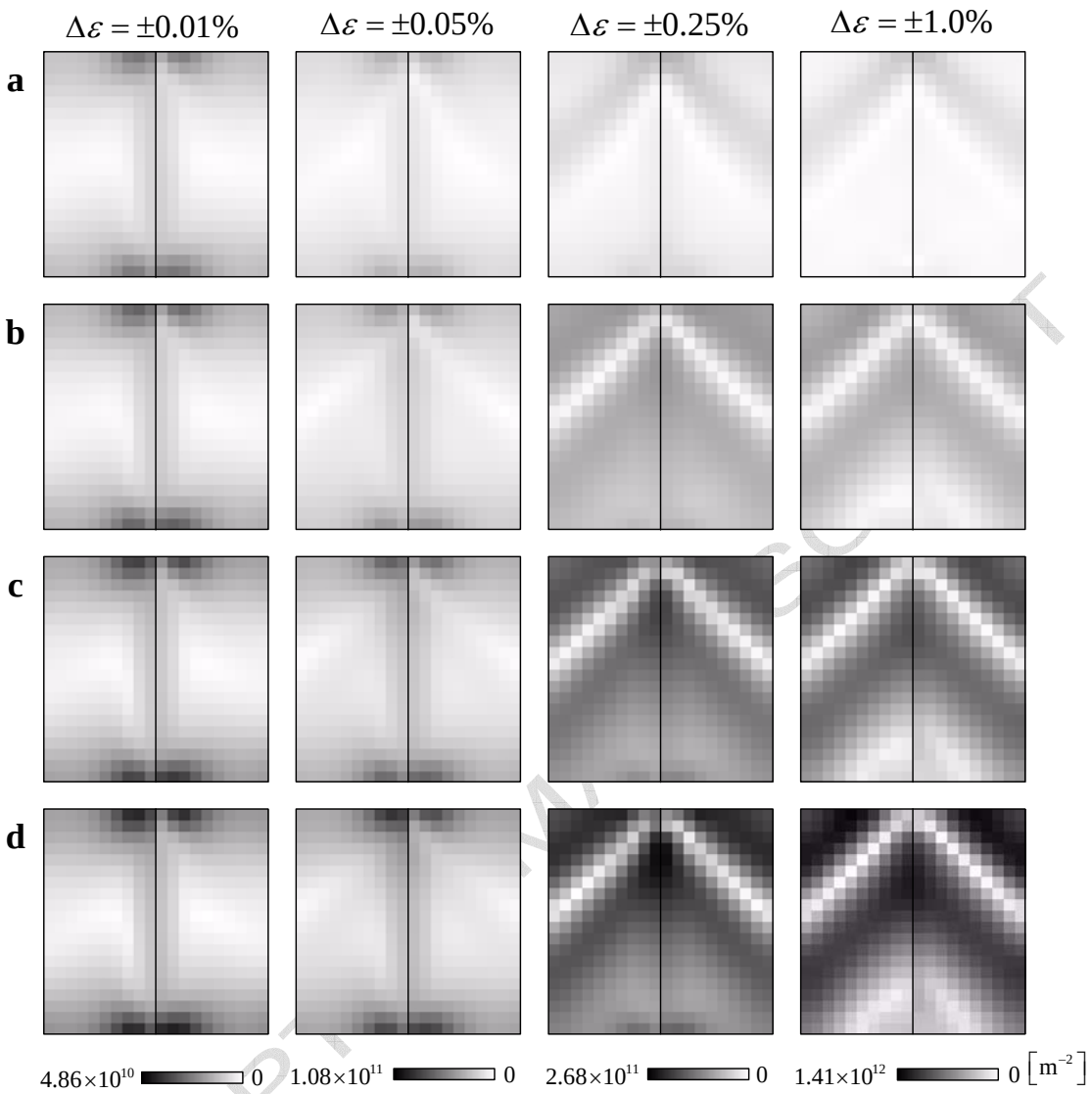

Fig.11 Evolution of GND norm density distribution on primary slip system (B4) during cyclic loading calculated with elastic anisotropy (a) at 1st peak stress; (b) after 1cycle; (c) after 5cycles; (d) after 10cycles.

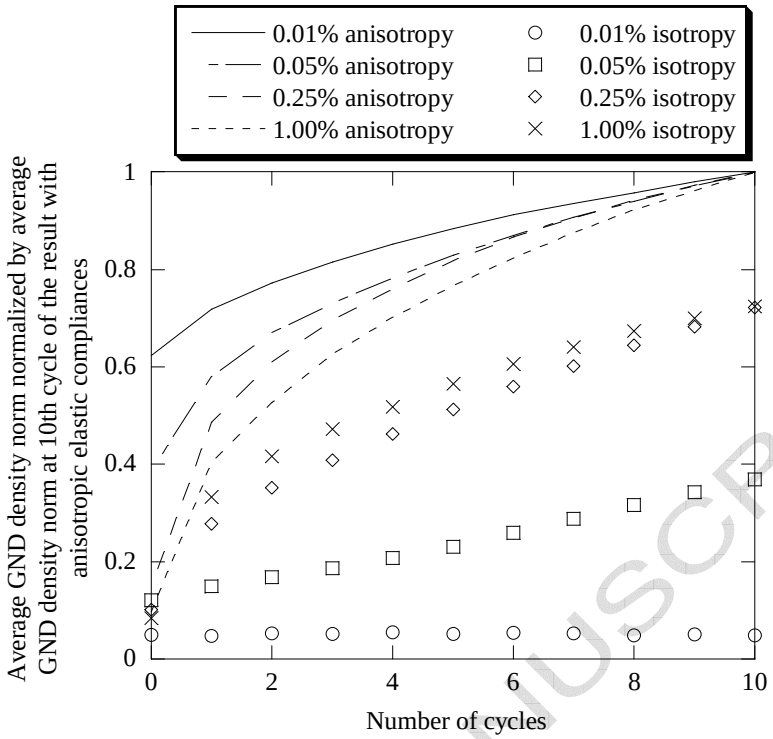

Fig.12 The effect of elastic anisotropy on the increase in average GND density norm

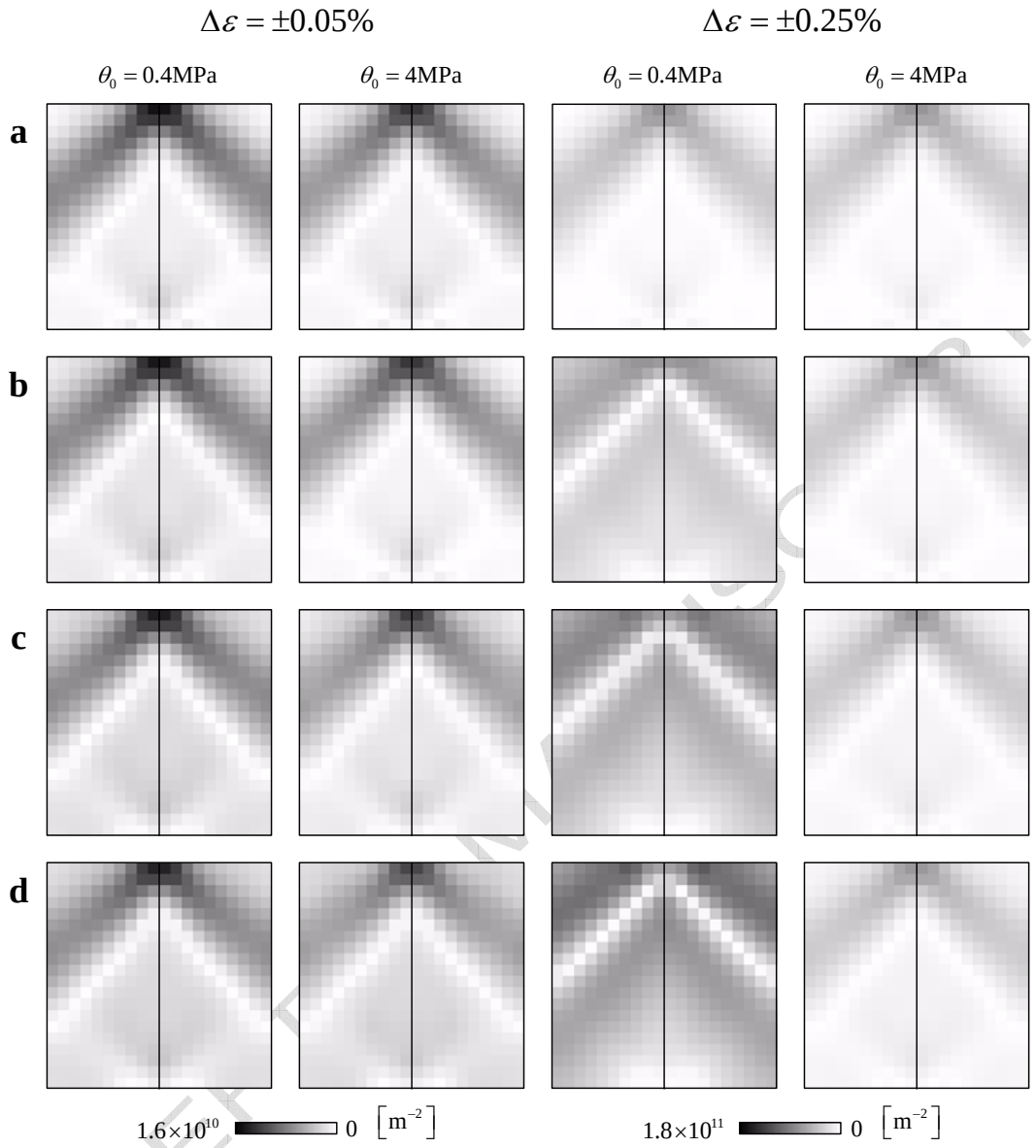

Fig.13 Evolution of GND norm density distribution on primary slip system (B4) during cyclic loading calculated with non-zero lattice friction stress θ_0 in Eq.(5) (a) at 1st peak stress; (b) after 1cycle; (c) after 5cycles; (d) after 10cycles.

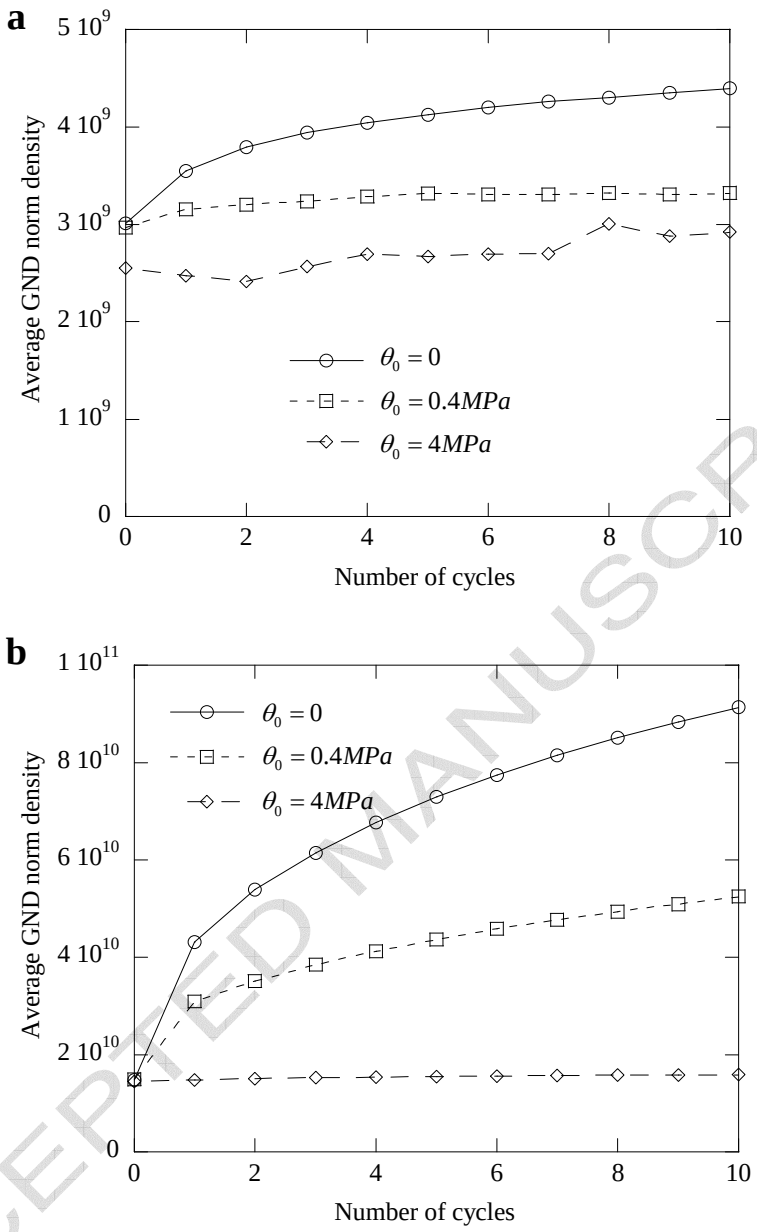

Fig.14 The effect of non-zero lattice friction stress on the increase in average GND density norm (a) strain amplitude 0.05%; (b) strain amplitude 0.25%

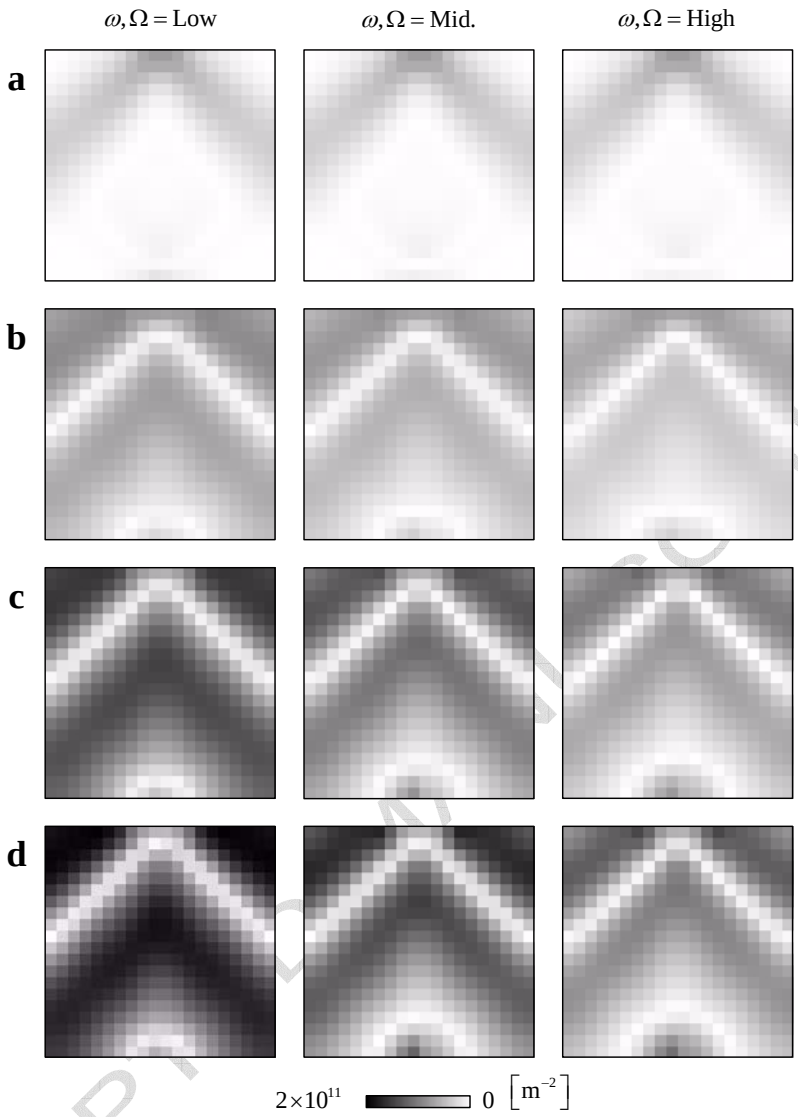

Fig.15 Effect of the off-diagonal component of interaction matrix $\Omega^{(n\neq m)}$ and the off-diagonal components except for co-planar of weight matrix $\omega^{(n\neq m)}$ on evolution of GND norm density distribution on primary slip system (B4) (a) at 1st peak stress; (b) after 1cycle; (c) after 5cycles; (d) after 10cycles.

Table 3 Interaction matrix and weight matrix parameters

	Low	Mid.	High
$\Omega^{(nm)}$ n=m	1	1	1
$\Omega^{(nm)}$ n≠m	0.98	1.01	1.04
$\omega^{(nm)}$ n=m or co-planar	0	0	0
$\omega^{(nm)}$ n≠m	0.98	1.01	1.04